Cronfa - Swansea University Open Access Repository

_____

This is an author produced version of a paper published in :
Science

_____

Cronfa URL for this paper:

_____

Paper:

_____

Reverse glacier motion during iceberg calving and the cause of glacial earthquakes

Authors:

T. Murray[1]*, M. Nettles[2], N. Selmes[1], L. M. Cathles[3], J. C. Burton[4], T. D. James[1], S. Edwards[5], I. Martin[5], T. O'Farrell[6], R. Aspey[6], I. Rutt[1], and T. Baugé[7]

Affiliations:

[1]Glaciology Group, Department of Geography, College of Science, Swansea University, Swansea SA2 8PP, UK

[2]Lamont-Doherty Earth Observatory, Columbia University, New York, NY 10964 USA

[3]Department of Atmospheric, Oceanic and Space Sciences, University of Michigan, Ann Arbor, MI 48109 USA

[4]Department of Physics, Emory University, Atlanta, GA 30322 USA

[5]School of Civil Engineering and Geosciences, Newcastle University, Newcastle upon Tyne, NE1 7RU, UK

[6]Department of Electronic and Electrical Engineering, University of Sheffield, Sheffield S1 3JD, UK

[7]Thales UK, Research & Technology, Worton Drive, Reading, Berkshire, RG2 0SB, UK

*Correspondence to: t.murray@swansea.ac.uk

Abstract

Nearly half of Greenland's mass loss occurs through iceberg calving, but the physical mechanisms operating during calving are poorly known and *in situ* observations are sparse. We show that calving at Greenland's Helheim Glacier causes a minutes-long reversal of the glacier's horizontal flow and a downward deflection of its terminus. The reverse motion results from the horizontal force caused by iceberg capsize and acceleration away from the glacier front. The downward motion results from a hydrodynamic pressure drop behind the capsizing berg, which also causes an upward force on the solid Earth. These forces are the source of glacial earthquakes, globally detectable seismic events whose proper interpretation will allow remote sensing of calving processes occurring at increasing numbers of outlet glaciers in Greenland and Antarctica.

Main text

One third to one half of Greenland's total mass loss occurs through iceberg calving at the margins of tidewater-terminating glaciers (*1, 2*). Recent, rapid changes in glacier dynamics are associated with increased calving rates (*3-5*) and increased rates of glacial earthquakes (*6*). At large glaciers with near-grounded termini, calving typically occurs when buoyancy forces cause icebergs the full thickness of the glacier to capsize against the calving front (*6-9*). This type of calving is associated with glacial earthquakes (*6, 7, 10*), long-period seismic emissions of magnitude ~5 that are observed globally (*11*). The earthquakes have expanded northward and increased seven-fold in number during the last two decades (*6, 12, 13*), tracking changes in glacier dynamics, the retreat of glacier fronts, and increased mass loss (*6, 14*). Buoyancy-driven calving represents an increasingly important source of dynamic mass loss (*6-8*) as glacier fronts throughout Greenland have retreated to positions near their grounding lines (*15*). However, due to the difficulty of instrumenting the immediate near-terminus region of these highly active glaciers, few direct observations of the calving process are available, limiting development of the deterministic calving models required for improved understanding of controls on dynamic ice-mass loss. Detailed knowledge of the glacial-earthquake source would allow quantification of calving processes at a large class of Greenland glaciers as well as in several regions of Antarctica (*13*).

Agreement on the source mechanism of glacial earthquakes is limited. Analysis of long-period seismic data shows that a sub-horizontal force acts approximately perpendicular to the glacier calving front during the earthquakes (*6, 13*). The observed seismic signal is generated over a period of one minute or more (*6, 11, 16*), much longer than the source duration for tectonic earthquakes of similar size (*17*). Some authors favor a model in which momentum transfer produces a force acting in the upglacier and then downglacier directions as a newly calved iceberg overturns, accelerates away from the calving front and subsequently decelerates (*6, 10, 13, 18*). Others suggest that the seismic signal arises from the iceberg scraping along the calving front or fjord bottom (*7*) or colliding with the glacier terminus (*19*). Hydrodynamic interactions with fjord water may be important (*20*) but are little explored. Analytical investigations admit more than one possible mechanism for the earthquakes (*18*), and no persuasive explanation has been presented for the vertical component of the earthquake force. Here, we combine geodetic, seismic and laboratory data to identify the forces acting during calving at large glaciers and document the source of the associated seismic signals.

We recorded geodetic data at the calving margin of Helheim Glacier (Fig. 1) (*9*), a major outlet of the Greenland Ice Sheet, during 55 days in July-September 2013. A wireless network of on-ice GPS sensors (*21*) captured glacier motion with cm-level accuracy at positions very close to the calving front at a high temporal sampling rate (*22*). Hourly images from two cameras located ~4 km down-fjord from and looking at the calving front were used in stereo configuration to obtain the 3D geometry of the calving front and calved icebergs (*8, 22*). Data from the global seismographic network were analysed for the same time period to identify glacial earthquakes (*13, 23*) and obtain source parameters (*11*) including the orientation of the force active during the earthquake and the amplitude and centroid time, t_c, of a centroid-single-force (CSF) history of prescribed shape (*22*).

The glacier retreated ~1.5 km in a series of calving events during the observing period. We identified ten large calving events from the camera images. All coincided with glacial earthquakes; in two cases, two earthquakes occurred between subsequent images. During the earthquakes, the region near the calving front shows a dramatic reversal of flow, moving upglacier for several minutes while simultaneously moving downward (Fig. 2, Fig. S1). The horizontal and vertical motion then rebound rapidly.
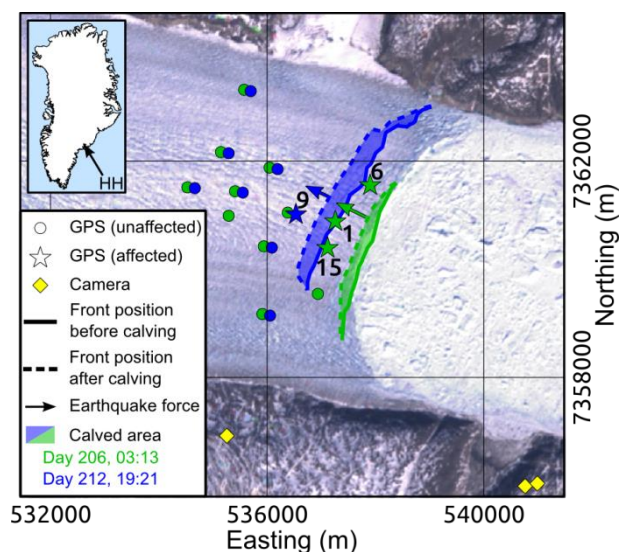
Fig. 1. Helheim Glacier, position of sensors, and seismic force directions. Location of GPS sensors and icebergs calved at Helheim Glacier (HH) for glacial-earthquake events at 03:13 DOY 206 2013 and 19:21 DOY 212 2013, superimposed on Landsat 7 image from DOY 167 2013. 'Affected' sensors exhibit earthquake-related deflections. Scan-line-corrector failure stripes have been removed for clarity. Glacier flow from left to right; bright white mélange (mix of iceberg fragments and sea ice) can be seen in front of calving margin. Calving-front positions obtained from photogrammetric DEMs derived from cameras. Times are UTC, positions are meters UTM zone 24N.
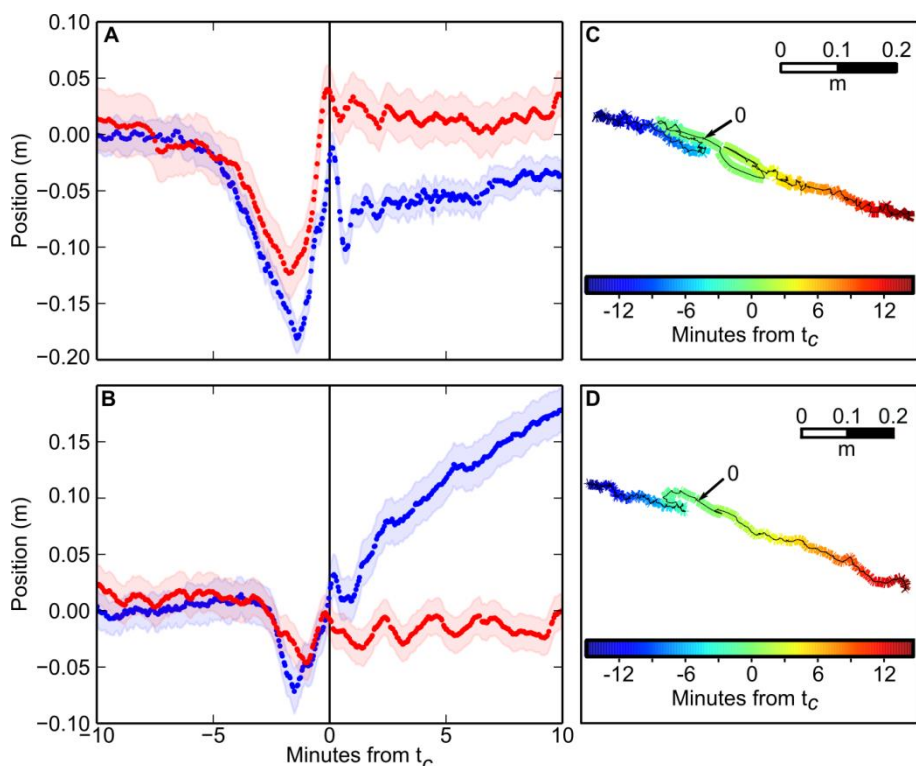
Fig. 2. Response of GPS sensors on glacier at the time of glacial earthquakes. (A) Sensor 1 at 03:13 on DOY 206 2013. (B) Sensor 9 at 19:21 on DOY 212 2013. Blue dots show detrended along-flow displacement, red dots show height. Shading shows 1σ position errors. Earthquake centroid time t_c. Horizontal displacement has trend from 30-10 mins before t_c removed (A=28.9 m/day, B=24.6 m/day). Height has mean removed. (C) and (D) Plan view of GPS traces shown in (A) and (B) during 30 minutes around t_c, marked as 0.

Observations from a glacial earthquake occurring on Day of Year (DOY) 206 at 03:13:47 are shown in Figs. 2A and 2C. Analysis of camera images indicates ice loss of 0.461 ± 0.009 km^2 (Fig. 1) at a location of ice thickness 0.79 km, yielding an iceberg volume of 0.36 km^3 with aspect ratio 0.23. The earthquake had CSF amplitude 0.24 x 10^{14} kg-m, with the force oriented 64°W (Fig. 1) and 9° above the horizontal. GPS sensor 1 (Fig. 1) showed a pre-earthquake flow speed of 29 m/day. Immediately prior to the earthquake centroid time, the sensor reversed its direction and moved upglacier at ~40 m/day (displacement 9 cm) and downward (displacement 10 cm). The reversed motion was sustained for ~200 seconds and was followed by a downglacier rebound at ~190 m/day (displacement 20 cm) and upward movement (16 cm) for ~90 seconds. Similar temporally coincident signals are seen on nearby sensors 6 and 15 (Fig. 1, Fig. S1).

Figures 2B and 2D show glacier deflection for a calving event on DOY 212 (Fig. 1). We observe similar responses for all glacial-earthquake / calving events during which GPS sensors recording data of adequate quality were located within 500 m of the calved block (a total of 9 glacial earthquakes and 8 image pairs). These events occurred on DOY 205, 206 (three events), 207, 211, 212, and 226 and are observed on multiple GPS sensors (further examples in Fig. S1).

The earthquake centroid times occur at or near the end of the glacier's rapid rebound phase, such that the upglacier earthquake force aligns in time with the reverse motion of the glacier. The horizontal glacier deflection is consistent with a model in which the reaction force on the glacier due to seaward acceleration of the newly calved iceberg compresses the glacier front elastically. The front then rebounds as the force decreases and reverses polarity during iceberg deceleration. The glacier front thus acts as a spring, compressing and re-extending in phase with the applied force, which is the horizontal component of the seismic source.

The downward deflection of the glacier front occurs in a region where vertical motion of the GPS sensors at tidal frequencies shows the glacier is ungrounded and seawater is present beneath it. Iceberg rotation is likely to cause a low-pressure zone in the opening cavity between the iceberg and the glacier front. This pressure decrease would lower the load on the bedrock, resulting in an upward force acting on the solid Earth, as observed in our seismic analysis. A pressure decrease near the calving front would apply a net downward force on the glacier terminus, lowering the glacier surface in a manner similar to that occurring twice each day when the ocean tides draw down the water level. At sensors experiencing earthquake deflections, we observe variations in vertical position due to the water tide of ~0.1 m per 1 m of tidal variation. The calving-related deflection of the glacier surface is ~0.1-0.16 m, suggesting a change in water pressure equivalent to a water-height change of ~1-1.6 m, or roughly 1-2 x 10^4 Pa.

No observations of pressure or water-level variations are available from the region in the fjord immediately in front of the glacier, where thick ice mélange (Fig. 1) prohibits instrumentation. However, results from analog laboratory experiments allow us to evaluate our inferences (*22*). A model glacier "terminus" was secured at one end of a water-filled tank, and plastic "icebergs" made from low-density polyethylene were placed flush against the terminus and allowed to capsize spontaneously under the influence of gravitational and buoyancy forces (*24*; Fig. 3). Sensors embedded in the model glacier terminus monitored pressure in the water column and the force exerted on the terminus during iceberg capsize.

The measured force on the terminus as the iceberg begins to capsize is oriented in the upglacier direction and slowly increases as the iceberg rotates. As the iceberg nears horizontal, the force decreases rapidly. Pressure at the terminus decreases as the iceberg
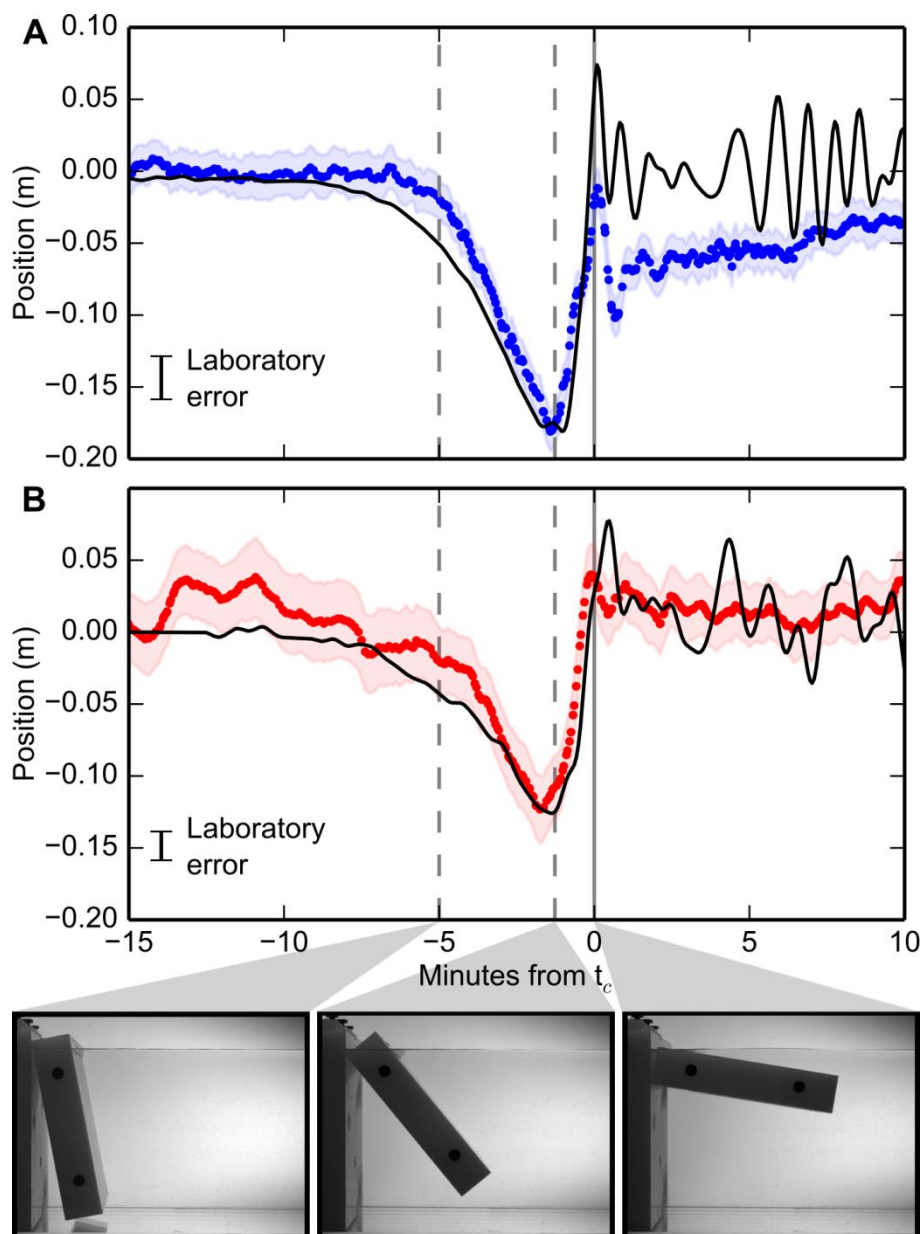
Fig. 3. Scaled laboratory data from glacier "terminus" during "iceberg" capsize event compared to field observations. (A) Horizontal displacement scaled from force (black line) compared to downflow GPS data (blue). (B) Vertical displacement scaled from pressure (black line) compared to vertical GPS data (red). Errors in laboratory data are standard deviation from repeated capsize events. GPS data as in Figure 2A. Photographs show stage of capsize at times marked by dashed lines and (solid gray line) t_c. Aspect ratio of model iceberg is 0.22.

rotates, increasing again as the iceberg nears horizontal. Once the iceberg loses contact with the terminus, the measured force and pressure begin to oscillate due to induced wave action in the tank.

We scaled up the measured forces and pressures to match the dimensions of icebergs calved at Helheim Glacier (Fig. 3). The laboratory data scale by powers of the ratio of the iceberg height in the field to the iceberg height in the laboratory (*20,24*). The scaled peak force agrees well with typical values inferred from earthquake analysis (~10^{11} N). The scaled peak pressure drop (~5×10^4 Pa) applied over an area corresponding to the iceberg's map-view dimensions yields an upward-directed

force consistent with the seismically inferred vertical force component, such that the total force acting on the solid Earth is oriented ~10° above the horizontal. Computation and inversion of synthetic seismograms from the scaled force and pressure data confirms the consistency of the laboratory model with real-world data.

We use the scaled force and pressure to predict the deformation of the terminus region (*22*). The total force F_{tot} per unit area A_F acting on the calving region produces a horizontal, linear deflection orthogonal to the calving front $F_{tot}/A_F = E\Delta L/L$, where E is the Young's modulus of glacial ice. The value of L is chosen to provide the best match to the glacier position data. This length-scale likely represents the distance from the terminus to the grounding zone. We model the ungrounded section of the glacier as an elastic beam of length L loaded by the vertical force due to the pressure drop. The inferred distances L are a few km, consistent with values estimated from GPS data.

Glacier displacements predicted from the scaled laboratory data for iceberg dimensions corresponding to a calving event on DOY 206 (Fig. 1, Fig. 2A) are shown in Fig. 3. Agreement with the observed glacier displacement is very good, particularly during the time over which the force acts in the upglacier direction (until the earthquake centroid time). After this time, the laboratory-derived prediction is dominated by oscillations of the water column in the tank, which does not contain the thick layer of ice mélange present in Helheim Fjord and expected to damp such high-frequency oscillations.

We conclude that as large icebergs rotate and accelerate away from the glacier calving front (Fig. 4), the reaction force, which is the horizontal component of the earthquake force, compresses the glacier front elastically, overcoming normal downglacier flow and temporarily reversing the motion of the glacier. Hydrodynamic interaction of the iceberg with the fjord water rapidly reduces pressure behind the rotating iceberg, resulting in an upward force on the solid Earth that is the vertical force observed in the earthquake. The lowered water pressure draws down the ungrounded glacier margin, pulling the glacier surface downward during the earthquake.
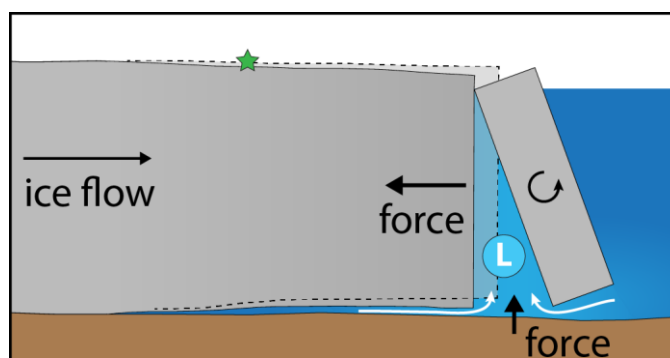
Fig. 4. Cartoon of glacier terminus during calving event. Glacier deflection caused by capsizing iceberg shown relative to initial position (dotted line). Acceleration of iceberg to right exerts a force in the upglacier direction (left), leading to reverse motion of the GPS sensors (green star). Reduced pressure behind the iceberg ("L") draws water from beneath the glacier and from the proglacial fjord, pulling the floating portion of the glacier downward and exerting an upward force on the solid Earth.

Our results document the forces active during an increasingly important class of calving events and definitively identify the processes that cause glacial earthquakes. This understanding of glacier calving and glacial earthquakes opens the potential for remote, quantitative characterisation of iceberg calving and calving rates, as well as improved models for ice-ocean interaction.

References and Notes

1. M. van den Broeke *et al.,* Partitioning recent Greenland mass loss. *Science* **326**, 984-986 (2009).

2. E. M. Enderlin *et al.,* An improved mass budget for the Greenland ice sheet. *Geophys. Res. Lett.* **41**, 866-872 (2014).

3. I. Joughin, W. Abdalati, M. Fahnestock, Large fluctuations in speed on Greenland's Jakobshavn Isbræ glacier. *Nature* **432**, 608-610 (2004).

4. A. Luckman, T. Murray, R. de Lange, E. Hanna, Rapid and synchronous ice-dynamic changes in East Greenland. *Geophys. Res. Lett*. **33**, L03503 (2006).

5. I. M. Howat, I. Joughin, T. A. Scambos, Rapid changes in ice discharge from Greenland outlet glaciers. *Science* **315**, 1559-1561 (2007).

6. S. A. Veitch, M. Nettles, Spatial and temporal variations in Greenland glacial-earthquake activity, 1993-2010. *J. Geophys. Res.* **117**, F04007 (2012).

7. J. M. Amundson *et al.,* Glacier, fjord, and seismic response to recent large calving events, Jakobshavn Isbrae, Greenland. *Geophys. Res. Lett.* **35**, L22501 (2008).

8. T. D. James, T. Murray, N. Selmes, K. Scharrer, M. E. O'Leary, Buoyant flexure and basal crevassing in dynamic mass loss at Helheim Glacier. *Nature Geosci.* **7**, 593-596 (2014).

9. T. Murray *et al.,* Dynamics of glacier calving at the ungrounded margin of Helheim Glacier, south-east Greenland. *J. Geophys. Res.* **120** (2015), doi:10.1002/2015JF003531.

10. M. Nettles *et al.,* Step-wise changes in glacier flow speed coincide with calving and glacial earthquakes at Helheim Glacier, Greenland. *Geophys. Res. Lett.* **35**, L24503 (2008).

11. G. Ekström, M. Nettles, G. A. Abers, Glacial earthquakes. *Science* **302**, 622-624 (2003).

12. G. Ekström, M. Nettles, V. C. Tsai, Seasonality and increasing frequency of Greenland glacial earthquakes. *Science* **311**, 1756-1758 (2006).

13. M. Nettles, G. Ekström, Glacial earthquakes in Greenland and Antarctica. *Ann. Rev. Earth Planet. Sci.* **38**, 467-491 (2010).

14. I. Joughin *et al.,* Ice-front variation and tidewater behavior on Helheim and Kangerdlugssuaq Glaciers, Greenland. *J. Geophys. Res.* **113,** F01004 (2008).

15. I. M. Howat, A. Eddy, Multi-decadal retreat of Greenland's marine-terminating glaciers. *J. Glaciol.* **57**, 389-396 (2011).

16. V. C. Tsai, G. Ekström, Analysis of glacial earthquakes. *J. Geophys. Res.* **112**, F03S22 (2007).

17. G. Ekström, E. R. Engdahl, Earthquake source parameters and stress distribution in the Adak Island region of the central Aleutian Islands, Alaska. *J. Geophys. Res*. **94**, 15,499-15,519 (1989).

18. V. C. Tsai, J. R. Rice, M. Fahnestock, Possible mechanisms for glacial earthquakes. *J. Geophys. Res.* **113**, F03014 (2008).

19. F. Walter *et al.,* Analysis of low-frequency seismic signals generated during a multiple-iceberg calving event at Jakobshavn Isbræ, Greenland. *J. Geophys. Res*. **117**, F01036 (2012).

20. J. M. Amundson, J. C. Burton, S. Correa-Legisos, Impact of hydrodynamics on seismic signals generated by iceberg collisions. *Ann. Glaciol.* **53**, 106–112 (2012).

21. I. Martin *et al.,* High-resolution sensor network for monitoring glacier dynamics. *IEEE Sensors J.* **14**, 3926-3931 (2014).

22. Materials and methods are available as supplementary materials on *Science* Online.

23. G. Ekström, Global detection and location of seismic sources by using surface waves. *Bull. Seismol. Soc. Am*. **96**, 1201-1212 (2006).

24. J. C. Burton *et al.,* Laboratory investigations of iceberg capsize dynamics, energy dissipation and tsunamigenesis. *J. Geophys. Res.* **117**, F01007 (2012).

25. H. Kawakatsu, Centroid single force inversion of seismic waves generated by landslides. *J. Geophys. Res.* **94**, 12363-12374 (1989).

26. A. M. Dziewonski, D. L. Anderson, Preliminary reference Earth model. *Phys. Earth Planet. Inter*. **25**, 297-356 (1981).

27. T. D. James, T. Murray, N. E. Barrand, S. L. Barr, Extracting photogrammetric ground control from lidar DEMs for change detection. *Photogramm. Rec.* **21,** 310-326 (2006).

28. C. Leuschen, C. Allen, IceBridge MCoRDS L3 Gridded Ice Thickness, Surface, and Bottom, Version 2, Helheim_2008_2012_Composite. Boulder, Colorado USA: NASA DAAC at the National Snow and Ice Data Center. http://nsidc.org/data/irmcr3.html (2013).

29. J. F. Zumberge, M. B. Heflin, D. C. Jefferson, M. M. Watkins, F. H. Webb, Precise point positioning for the efficient and robust analysis of GPS data from large networks. *J. Geophys. Res.* **102**, 5005-5017 (1997).

30. J. Saastamoinen, Contributions to the theory of atmospheric refraction. *Bull. Geodesique* **107**, 13-34 (1973).

31. J. Boehm, A. Niell, P. Tregoning, H. Schuh, Global Mapping Function (GMF): A new empirical mapping function based on numerical weather model data. *Geophys. Res. Lett.* **33**, L07304 (2006).

32. F. Lyard, F. Lefevre, T. Letellier, O. Francis, Modelling the global ocean tides: modern insights from FES2004. *Ocean Dynamics* **56**, 394-415 (2006).

33. G. Petit, B. Luzum, Eds., IERS Conventions (IERS Technical Note 36, Verlag des Bundesamts für Kartographie und Geodäsie, Frankfurt am Main, 2010).

34. W. Bertiger *et al*., Single receiver phase ambiguity resolution with GPS data. *J. Geod.* **84**, 327-337 (2010).

35. G. Chen, GPS kinematic positioning for the airborne laser altimetry at Long Valley, California. Ph.D. thesis, Mass. Inst. of Technol., Cambridge (1998).

36. R. Dach *et al.,* GNSS processing at CODE: status report. *J. Geod*. **83**, 353-365 (2009).

37. J. C. Burton, L. M. Cathles, W. G. Wilder, The role of cooperative iceberg capsize in ice-shelf disintegration. *Ann. Glaciol.* **54**, 84-90 (2013).

38. I. H. Cho, M. H. Kim, Wave absorbing system using inclined perforated plates. *J. Fluid Mech.* **606**, 1-20 (2008).

39. D. R. MacAyeal, D. S. Abbot, O. V. Sergienko, Iceberg-capsize tsunamigenesis. *Ann. Glaciol.* **52**, 51-56 (2011).

40. D. G. Vaughan, Tidal flexure at ice shelf margins. *J. Geophys. Res.* **100**, 6213-6224 (1995).

41. E. Rignot, Tidal motion, ice velocity and melt rate at Petermann Gletscher, Greenland, measured from radar interferometry. *J. Glaciol.* **42**, 476-485 (1996).

Acknowledgments

Supplementary Materials

Materials and Methods

Figure S1

References (*25-41*)

Additional Data Table S1